energies

MDPI

Article

Multi-Parameter Collaborative Optimization of a Coaxial Pulse Tube Cryocooler Integrating Acoustic–Mechanical–Electrical Coupling and Physical Boundary Constraints

Ruming Liu [1], Changpei Zhuang [1], Chunjie Yan [1,*], Haipeng Du [1] and Bo Wang [2]

[1] Lanzhou Institute of Physics, China Academy of Space Technology, Lanzhou 730030, China; rumingliu1999@163.com (R.L.); zcpcast@163.com (C.Z.); interstellar19@163.com (H.D.)
[2] Cryogenic Center, Hangzhou City University, Hangzhou 310015, China; wangbo@hzcu.edu.cn
* Correspondence: chj_yan@163.com

Abstract

Complex parameter interactions and acoustic–mechanical–electrical (AcME) impedance mismatches restrict coaxial pulse tube cryocooler (CPTC) performance, whereas previous studies typically optimized isolated cold fingers without compressor dynamic coupling. This study proposes a physics-prior-driven collaborative optimization framework for an integrated AcME-coupled CPTC system. Random Forest screening first compresses the 16-dimensional space to 10 core variables. Across 250 initial samples, the Kriging surrogate achieves baseline determination coefficients of $R^2 = 0.9812$ for cooling capacity and $R^2 = 0.9663$ for exergy efficiency. Although initial active learning expands the dataset to 350 samples, uncalibrated frontier exploration still encounters boundary extrapolation errors, inducing solver divergence and an initial 21.82% exergy discrepancy. To prevent search oscillations across non-convergent domains, a sequential active learning loop dynamically couples Constrained Expected Improvement infilling with Pareto feedback, while a Support Vector Machine enforces a numerical solvability boundary ($P_{safe} \geq 0.85$) alongside a power factor threshold ($PF \geq 0.95$). Computations deploy an 11-node coarse grid for search iterations and a 50-node fine grid for thermodynamic evaluation. Under fine-grid validation at 80 K, net cooling capacity reaches 14.41 W, and exergy efficiency increases from 14.65% to 17.65%, establishing a verifiable methodology for coupled thermodynamic systems.

Keywords: coaxial pulse tube cryocooler; acoustic–mechanical–electrical coupling; data-driven optimization; Kriging model; exergy analysis

Check for updates

Academic Editor: Zacharie Tamainot-Telto

Received: 21 August 2026
Revised: 22 September 2026
Accepted: 22 September 2026
Published: 30 September 2026

Copyright: © 2026 by the authors. Licensee MDPI, Basel, Switzerland. This article is an open access article distributed under the terms and conditions of the Creative Commons Attribution (CC BY) license.

1. Introduction

Since the discovery of the pulse tube effect by Gifford and Longsworth in 1964 [1], pulse tube cryocoolers (PTCs) have developed considerably. In recent years, technological breakthroughs in space PTCs have extended to high-frequency, lightweight, and efficient multi-stage precooling systems in the 20–40 K temperature range [2–4], as well as numerical explorations of novel structures such as active displacers [5]. Among various structural configurations, coaxial pulse tube cryocoolers (CPTCs) feature no moving parts at the cold end, offering advantages of reliability and low vibration, making them a suitable candidate for aerospace and superconducting applications. Key developments in this field include the 1.3 W@77 K miniature cryocooler developed by Northrop Grumman Space Technology (NGAS) [6,7], and the large-cooling-capacity (500 W@80 K) [8] or high-efficiency (15.9% relative Carnot efficiency) [9,10] models proposed by the Chinese Academy of Sciences.

As the demand for equipment miniaturization and higher power density in space exploration continues to increase, the component coupling issues involving the compressor, regenerator, and phase-shifting mechanism have emerged as a performance limiting factor. However, while increasing the operating frequency enhances the power density, it also complicates impedance matching and increases entropy production, necessitating an adjustment of the regenerator geometry and global operating conditions [11–16]. Fundamental studies by researchers, such as Wakeland [17], Swift [18], Radebaugh [11], Dai [19], and Gan [20], have explored these matching mechanisms from the perspectives of energy conservation and acoustic impedance.

Recent studies have utilized optimization strategies, such as response surface methodology (RSM) and Kriging, to improve cryocooler performance [21–27]. However, these applications typically focus on the local optimization of four to six geometric parameters for isolated cold fingers, without accounting for the dynamic coupling of the acoustic–mechanical–electrical (AcME) system. As summarized in Table 1, scaling the optimization to an integrated AcME whole system expands the design space to 10 dimensions, introducing two primary methodological challenges.

Table 1. Methodological comparison between previous optimization studies and the proposed framework.

Reference/Study	System Scope	Variable Scale	Surrogate Modeling Strategy	Boundary Constraint	Applicability and Quantitative Performance
Rout et al. (2014, 2015) [21,22]	Cold finger and passive phase-shifters	4–7 variables	Static RSM	Unconstrained	Applicable to structural thermodynamics; lacks compressor dynamic coupling.
Panda et al. (2019, 2020) [23,24]	Cold finger and passive phase-shifters	4–8 variables	PSO/ANN	Unconstrained	Focuses on uncoupled thermodynamics; ignores electrical-mechanical resonance matching.
Zhao, Geng, Wang et al. (2023, 2024) [25–27]	Cold finger and phase-shifting systems	4–6 variables	Static Kriging	Unconstrained	Effective for uncoupled components; exhibits precision limits in cross-domain spaces.
Proposed Framework (This study)	AcME whole system	10 core variables (Screened from 16-D AcME space via RF)	Sequential Kriging (Active learning + Pareto feedback) + Constrained NSGA-II	Probabilistic SVM boundary + PF safeguard	Resolves cross-domain AcME matching; eliminates solver divergence; coarse-grid Pareto error suppressed to <0.38%.

First, variations in the microscopic geometric dimensions of the cold finger trigger a nonlinear drift in acoustic impedance, which disrupts the impedance matching of the upstream compressor. When high-dimensional algorithms conduct unconstrained global exploration, they may generate parameter combinations that cause AcME impedance mismatch. Under such mismatched conditions, the system's thermodynamic responses enter nonlinear regions, increasing the risk of surrogate model extrapolation distortion. Furthermore, the PF of mature models typically resides in a low-gradient plateau region. Unconstrained global exploration within these intervals reduces computational efficiency. Therefore, rather than serving as an optimization objective, a global power factor threshold ($PF \geq 0.95$) is introduced as a robustness safeguard against extrapolation. This physics-prior constraint filters out mismatched configurations, ensuring that the surrogate model navigates within a mathematically reliable domain, while enabling the NSGA-II algorithm to concentrate on the trade-off between cooling capacity and exergy efficiency.

Second, while a well-conditioned 10-dimensional parameter space enables satisfactory global fitting across uniform Latin Hypercube samples, uniform sampling remains spatially sparse along multi-variable boundaries and the narrow Pareto trade-off corridor. During evolutionary iterations, unrefined surrogates are susceptible to localized extrapolation overestimation, guiding optimization algorithms toward numerical artifacts that diverge upon Sage simulation (as demonstrated in Section 3.3).

To address these challenges, the proposed physics-prior-driven collaborative optimization framework operates through a progressive three-phase mechanism. First, the Random Forest (RF) algorithm evaluates out-of-bag feature importance to screen the 16-dimensional initial space down to 10 core variables, eliminating low-sensitivity dimensions to mitigate the curse of dimensionality. Building upon this subspace, a Constrained Expected Improvement (CEI) active learning strategy dynamically reinforces sample coverage along high-gradient frontiers to suppress local extrapolation errors. During the subsequent NSGA-II optimization, a Support Vector Machine (SVM) classifier establishes a numerical solvability boundary ($P_{\text{safe}} \geq 0.85$) to prevent exploring regions that trigger solver divergence or compression-space negative absolute pressure, while enforcing the power factor limit ($PF \geq 0.95$) as an extrapolation safeguard. Finally, an 11-node coarse grid is deployed for rapid iterative search, followed by a 50-node fine-grid evaluation to resolve steep temperature gradients and verify whole-system thermodynamic performance.

2. Numerical Model Construction and Multi-Parameter Collaborative Optimization Framework

2.1. Physical Modeling and Thermodynamic Evaluation Framework

2.1.1. Sage Physical Model Construction and Impedance Evaluation Mechanism

Figure 1 illustrates the structural schematic of the investigated CPTC. To balance computational efficiency and the accuracy of thermodynamic performance prediction during large-scale sample evaluation, a one-dimensional (1D) numerical model was established based on the Sage simulation platform (Figure 2). As a 1D numerical tool in the field of thermoacoustic refrigeration, Sage reflects the acoustic flow resistance, heat transfer, and local energy consumption within relevant components. Previous studies have verified that physical simulation models built on this platform can output alternating thermodynamic responses, making them applicable for global search and design characterization of system parameters in conjunction with heuristic algorithms such as genetic algorithms [22]. The geometric dimensions and material configurations of the core components are detailed in Table 2.

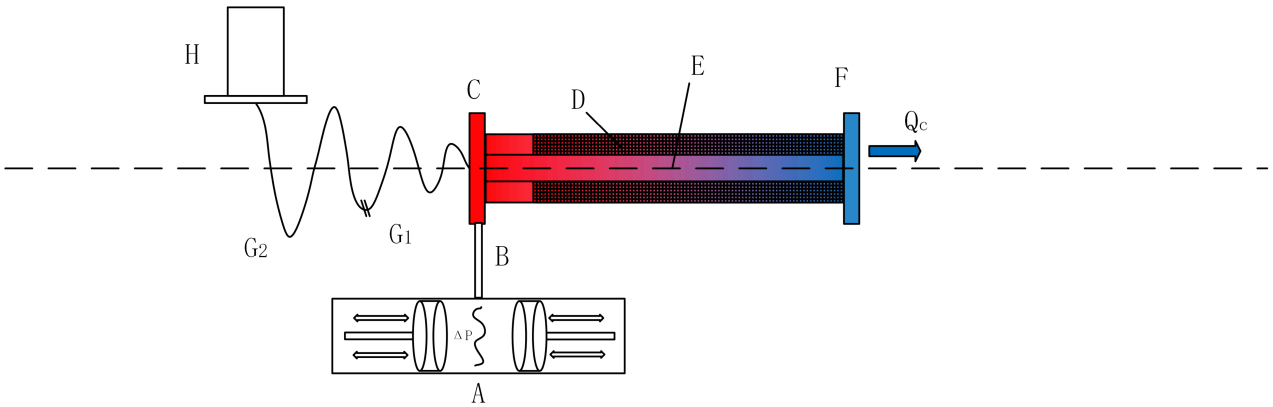


Figure 1. Schematic model of the coaxial pulse tube cryocooler. A: compressor, B: transfer tube, C: hot heat exchanger, D: regenerator, E: pulse tube, F: cold heat exchanger, G1, G2: two-stage inertance tubes, H: reservoir.

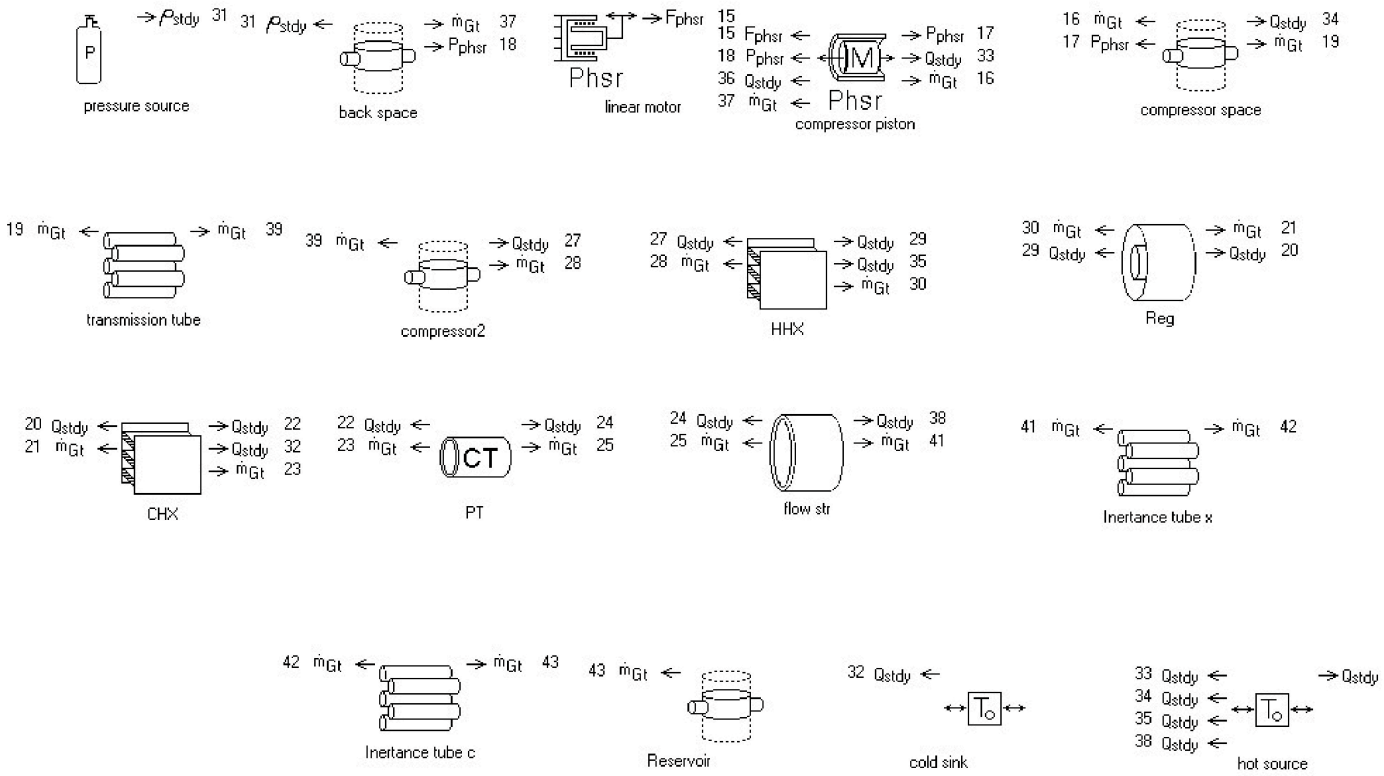


Figure 2. One-dimensional modular thermoacoustic network model of the integrated CPTC established in the Sage simulation platform. Arrows indicate directional alternating mass/acoustic power flows; numeric ports denote boundary couplings between adjacent sub-components.

Table 2. Geometry details and wall material of the proposed numerical model.

Component	Symbol	Diameter (mm)	Length (mm)	Material
Compressor	A	82	205	*
Transfer tube	B	4.2	100	SS304
Hot heat exchanger	C	10	11	Copper
Regenerator	D	11.4 (D_{in}) 22 (D_{out})	40	Titanium
Pulse tube	E	11.4	50	Titanium
Cold heat exchanger	F	10	5.4	Copper
Inertance tube 1	G1	3	1540	SS304
Inertance tube 2	G2	4	2050	SS304
Reservoir	H	*	*	*

Note: * indicates that these geometric parameters are defined by the equivalent volume/swept volume in the simplified 1D model.

To balance computational cost and solution accuracy, a multi-fidelity modeling concept was introduced in the spatial discretization solution [28]. Based on the grid independence test, the axial control volume nodes for the core components with severe axial temperature gradients and complex nonlinear dissipation (the regenerator and pulse tube) were refined from 11 (used during high-throughput optimization) to 50 for the final exergy verification, while the node discretization for the remaining components remained unchanged:

- Coarse-grid stage (11 nodes): Deployed during the feature ranking, surrogate model construction, and optimization stages to maintain the efficiency of iterations.
- Fine-grid stage (50 nodes): Utilized for final whole-system performance verification and exergy analysis. By refining the local grids to reduce numerical residuals, this

stage adheres to the entropy generation minimization (EGM) principle [29] and thermoacoustic loss theory [18,30], decoupling irreversible losses such as microscopic viscous dissipation, radial heat transfer, and axial heat conduction.

The model sets the cold-end heat exchanger temperature to 80 K and the hot-end heat rejection temperature to 300 K. The working fluid is 3 MPa ideal helium (using the built-in gas.dta physical property database in Sage). The linear compressor operates under a fixed-current model assumption (constant driving current I_{rms} and fixed coil resistance R_e). Under this condition, the coil Joule dissipation remains invariant, and the variation in gross active electrical input power (W_e) is governed by the electromechanical conversion power ($W_{e,net} = \alpha I_{rms} u_{rms} \cos\psi$). Sage captures the flow resistance, heat transfer, and internal losses in unsteady alternating flows. To ensure numerical stability, the allowable variation step size per iteration was adjusted toward the stable regime, and the convergence target error was set to 10^{-11}. Detailed graphical solver settings and the input deck parameters are provided in Figure S1 and Section S1 of the Supplementary Materials, while the corresponding 50-node model files are available in the accompanying repository.

To model the impedance coupling relationship during actual system operation and avoid the limitations of evaluating the linear compressor in isolation, an equivalent AcME impedance network covering the entire "compressor-cold finger" system was constructed (Figure 3) based on the physical model proposed by Gan et al. [17,20].

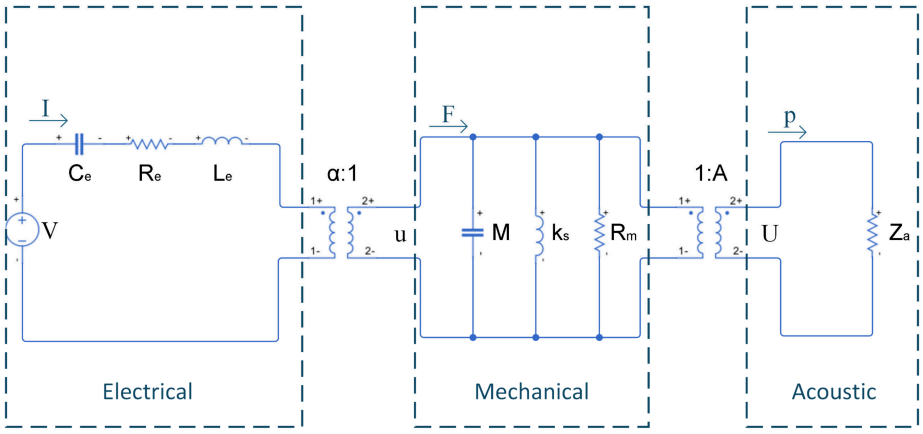


Figure 3. Equivalent AcME impedance network model of the compressor-driven cold finger.

In the complex frequency domain, the electrical, mechanical, and acoustic domains are connected by complex impedances, with the inherent impedances defined, respectively, as:

$$Z_e = R_e + j\omega L_e = R_e + jX_e \tag{1}$$

$$Z_m = R_m + j(\omega M - k_s/\omega) = R_m + jX_m \tag{2}$$

$$Z_a = \frac{p}{U} = R_a + jX_a \tag{3}$$

To analyze the underlying physical mechanism of the macroscopic acoustic feedback impedance Z_a in Equation (3), harmonic approximation theory [31] is introduced to evaluate the microscopic mass flow evolution inside the cold finger (Figure 4). In the complex frequency domain, setting the alternating pressure P as the real-axis reference, the local volume charging and discharging effects exhibit capacitive characteristics (leading the pressure wave by 90°). These segmented capacitive phase shifts, induced by the dead

volume, regenerator void volume, and pulse tube volume, satisfy the following mass conservation relationships:

$$\frac{-P_0 U_{co}}{RT_{co}} = \dot{m}_{reg,h} + \frac{j\omega PV_{Dead}}{RT_{co}} + \frac{j\omega PV_{co}}{2RT_{co}} \tag{4}$$

$$\dot{m}_{reg,h} = \dot{m}_{reg,c} + \frac{j\omega PV_{reg}}{RT_{reg}} \tag{5}$$

$$\dot{m}_{pt,c} = \frac{T_h}{T_c}\dot{m}_{pt,h} + \frac{j\omega PV_{pt}}{\gamma RT_c} \tag{6}$$

where P_0 is the average pressure; U_{co} and V_{co} are the piston volume flow rate and alternating compression chamber volume, respectively; V_{Dead}, V_{reg}, and V_{pt} are the inactive dead volume, regenerator void volume, and pulse tube volume; $\dot{m}_{reg,h}$ and $\dot{m}_{reg,c}$ are the mass flow rates at the hot and cold ends of the regenerator; $\dot{m}_{pt,c}$ and $\dot{m}_{pt,h}$ are the mass flow rates at the cold and hot ends of the pulse tube; and γ is the specific heat ratio.

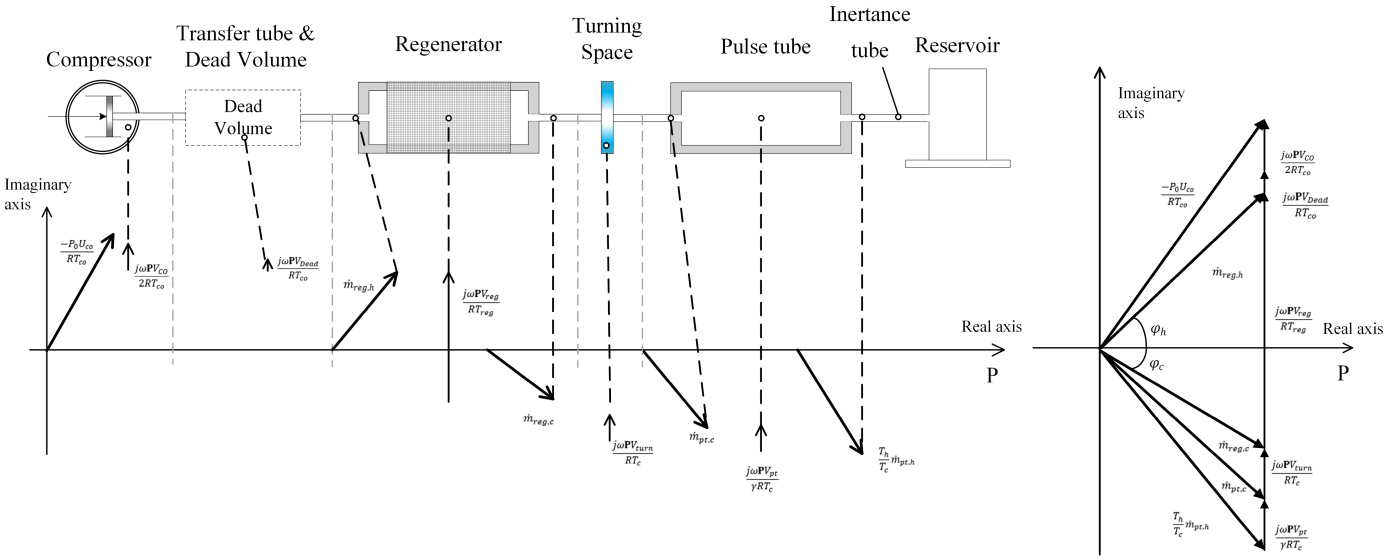


Figure 4. Phasor distribution of mass flow rates across the cold finger components in the CPTC.

The phasor analysis indicates that the geometric volumes inside the cold finger introduce capacitive delays, which map macroscopically as an increase in the acoustic feedback reactance X_a (presenting a negative value) in Equation (3). In actual operation, this acoustic boundary interacts with other components; the mismatch of downstream acoustic impedance influences upstream matching. To illustrate this global AcME coupling mechanism, this study constructs a coupled phasor diagram (Figure 5) [32].

In the AcME coupled phasor diagram, the acoustic reactance X_a is integrated into the mechanical impedance network. When the inductive phase-shifting capability of the inertance tube is insufficient to offset the capacitive consumption downstream, the gas force vector deviates from the phase of the piston velocity. This phase shift in the mechanical domain affects the resonance equilibrium of the compressor, triggers back-electromotive force (back-EMF) distortion, and causes the driving current I to deviate from the phase of the supply voltage V across the electromagnetic coupling boundary, indicating a decrease in overall energy conversion efficiency. Based on the energy flow transfer relationship between the electromechanical coupling constant α and the piston area A, the equivalent total impedance Z of the system can be derived as:

$$Z = Z_e + \frac{\alpha^2}{A^2 Z_a + Z_m} = \left[R_e + \frac{R\alpha^2}{R^2 + X^2}\right] + j\left[X_e - \frac{X\alpha^2}{R^2 + X^2}\right] \tag{7}$$

Here, to simplify the acoustic–mechanical coupling term, the global equivalent mechanical resistance is defined as $R = R_m + A^2 R_a$, and the global equivalent mechanical reactance is $X = X_m + A^2 X_a$.

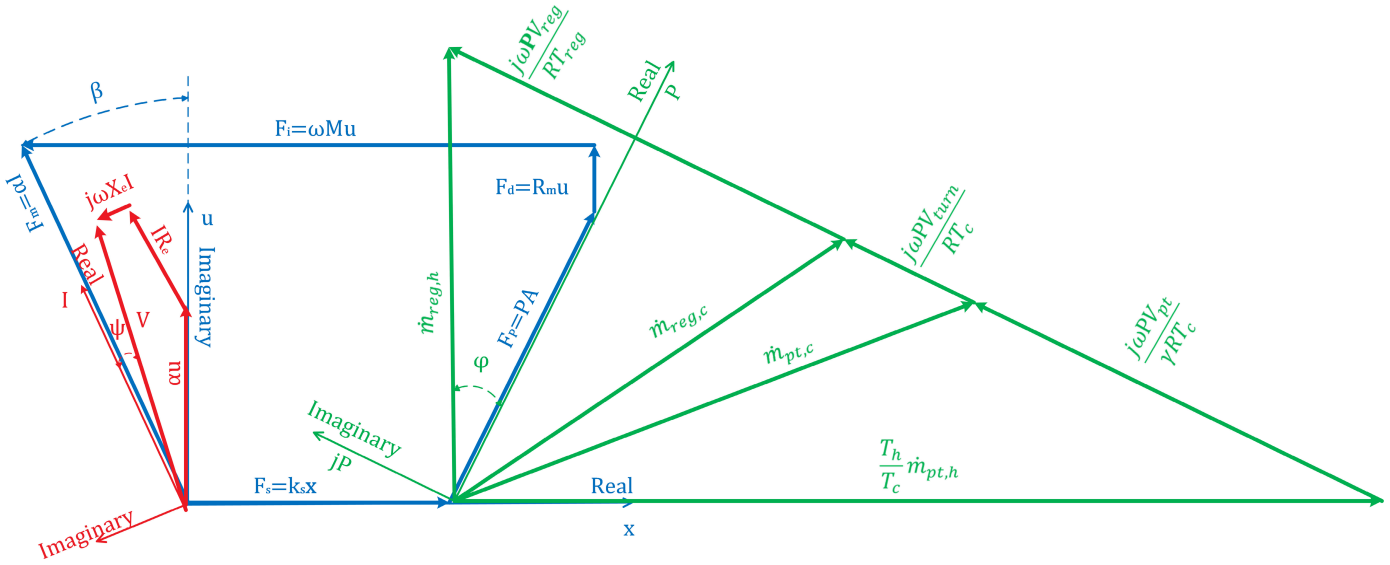


Figure 5. Global AcME-coupled phasor diagram illustrating the inter-domain dynamic equilibrium (red loop: electrical domain balance among voltage V, current I, and back-EMF αu with phase angle ψ; blue loop: mechanical domain force balance among electromagnetic force F_m, gas pressure force F_p, damping, stiffness, and inertia; green loop: acoustic domain mass flow continuity and phase angle φ relative to dynamic pressure P).

To regulate the reactive power increment caused by cross-domain mismatch, the PF is introduced as an evaluation metric [20]:

$$\cos\theta_{V-I} = \frac{1}{\sqrt{1 + \left[\frac{(R^2+X^2)X_e - X\alpha^2}{(R^2+X^2)R_e + R\alpha^2}\right]^2}} \tag{8}$$

From Equation (8), it can be seen that, limited by the motor inductance L_e, a high PF and optimal mechanical resonance ($X = 0$) are mutually exclusive events. For mature models, PF exhibits low sensitivity to minor parameter perturbations, residing in a zero-gradient plateau. Setting it as an active optimization objective forces redundant iterations in flat regions; therefore, this study defines it as a physical hard constraint ($PF \geq 0.95$). This a priori constraint acts as a robustness safeguard against extrapolation, allowing the multi-objective algorithm to focus completely on the thermodynamic trade-off between cooling capacity and overall exergy efficiency.

2.1.2. Macroscopic Thermodynamic Performance and Exergy Analysis Model

Although the global PF determines the state of cross-domain impedance matching from an electromechanical dynamics perspective, the CPTC, as a thermoacoustic energy conversion network, is evaluated primarily by its macroscopic cooling capacity and overall energy conversion efficiency.

During the alternating cycle, the linear compressor drives the piston to perform work, injecting energy into the cold finger network in the form of acoustic waves (alternating pressure and volume flow rate). After undergoing gas–solid heat transfer and viscous

dissipation inside the regenerator, as well as phase reconstruction by the phase-shifting mechanism, the acoustic work reversely pumps heat at the cold-end heat exchanger (CHX). Within one operating cycle, the net cooling capacity Q_c at the CHX is characterized as the difference between the mean alternating enthalpy flow and various irreversible heat leaks:

$$Q_c = \frac{1}{\tau}\oint_0^\tau (\dot{m}h)_c dt - \sum Q_{loss} \tag{9}$$

where $(\dot{m}h)_c$ is the transient enthalpy flow passing through the cold end, $\sum Q_{loss}$ is the sum of irreversible losses such as axial heat conduction, radiation, and non-uniform heat transfer.

Since a single cooling capacity metric cannot reflect the quality differences in energy conversion across different temperature zones, this study introduces the overall exergy efficiency (η_{ex}) as the core evaluation metric to comply with the second law of thermodynamics. Setting the ambient temperature $T_0 = 300$ K and the cold-end target temperature $T_c = 80$ K, the effective cold exergy (E_c) obtained by the CHX can be expressed as:

$$E_c = Q_c\left(\frac{T_0}{T_c} - 1\right) \tag{10}$$

Furthermore, the η_{ex} is defined as the ratio of the effective cold exergy to the total active electrical power input of the system, used to characterize the system's capability to suppress irreversible entropy productions in the cryogenic temperature region:

$$\eta_{ex} = \frac{E_c}{W_e} \tag{11}$$

During the high-dimensional optimization process, the system exhibits a thermodynamic trade-off: increasing the cooling capacity requires pushing higher mass flow rates and pressure ratios, which increases microscopic flow velocity within the channels. This causes an escalating viscous resistance exergy loss and heat transfer irreversibility, restricting the overall exergy efficiency. Conversely, over-suppressing local dissipation will limit the system's cooling output. The "cooling capacity vs. exergy efficiency" dilemma constitutes the motivation for introducing NSGA-II to solve the Pareto front.

2.2. Optimization Methods

2.2.1. Feature Importance Evaluation via Random Forest

To manage the 16-dimensional parameter space, an RF [33] algorithm utilizing the Bootstrap Aggregation framework (fixed at 1000 decision trees) is introduced to evaluate feature sensitivity. Using the out-of-bag (OOB) permutation predictor importance algorithm [34], the model parallelly trains target forests for cooling capacity and exergy efficiency. To eliminate statistical bias, the model executes 20 independent evaluation cycles with deterministic random seeds, outputting unbiased feature weights with a 95% confidence interval and reducing the design space to the top-10 core variables.

2.2.2. Kriging Surrogate Model Construction

A Kriging surrogate model is deployed to map the thermoacoustic response surface within the reduced 10-dimensional space. To capture the nonlinear gradient mutations near the system's extreme optimization boundaries, the covariance structure explicitly locks the correlation function to the Matern 5/2 kernel. This ensures second-order mean-square differentiability, mapping physical gradient changes without inducing oscillations during boundary extrapolation.

2.2.3. Active Learning Strategy Integrating Spatial Variance and Constrained Expected Improvement (CEI)

To address the cognitive uncertainty caused by sparse data in the 10-dimensional parameter space, this study deployed a batch active learning point-adding algorithm integrating physical spatial variance and CEI in the early stages of optimization. In each iteration, the algorithm first generates 10^5 virtual candidate points within the constrained space through Latin Hypercube Sampling (LHS) and then initiates a dual-track parallel sampling mechanism of "exploration" and "exploitation":

Global Exploration Path: Based on the surrogate model's prediction uncertainty $\sigma(x)$, K-Means clustering is used to extract 25 sampling points with the highest variance and overall spatial representativeness from the candidate pool, curbing overfitting in single-objective regions.

Directional Exploitation Path: Relying on the expected improvement in target exergy efficiency $EI_{Eff}(\mathbf{x})$, and combining it with the feasibility statistical probability $PoF(\mathbf{x})$ that the sample point satisfies the impedance safety constraint PF ≥ 0.95, a Constrained Expected Improvement function $CEI(\mathbf{x})$ is constructed to screen the top-25 high-quality solutions with low reactive power loss:

$$\mathrm{PoF}(\mathbf{x}) = \Phi\left(\frac{\mu_{\mathrm{PF}}(\mathbf{x}) - 0.95}{\sigma_{\mathrm{PF}}(\mathbf{x})}\right) \tag{12}$$

$$\mathrm{CEI}(\mathbf{x}) = \mathrm{EI}_{\mathrm{Eff}}(\mathbf{x}) \times \mathrm{PoF}(\mathbf{x}) \tag{13}$$

When a candidate point possesses high efficiency potential, but it violates the impedance matching laws such that its predicted PF is highly likely to fall below 0.95, its PoF value will approach 0, thereby directly terminating the evaluation of the CEI score for this point. This strategy effectively improved the iteration convergence speed of the Kriging model and reduced the workload.

2.2.4. Constrained Multi-Objective Optimization Based on SVM Data-Driven Numerical Solvability Boundary and Robust Decision Making

The NSGA-II algorithm [35] addresses the thermodynamic trade-off between cooling capacity and overall exergy efficiency using a progressive mechanism. The optimization hyperparameters for the NSGA-II algorithm are configured as follows: the initial population size is set to 200, the maximum number of generations to 200, and the Pareto fraction to 0.35. To prevent extrapolation divergence triggering thermoacoustic instability in physical simulations, dual thermodynamic physical extremum constraints and a Gaussian kernel SVM feasibility boundary are formulated into a unified mathematical model:

$$\text{Minimize} : f(\mathbf{x}) = [-Q_c(\mathbf{x}), -\max(0, \eta_{ex}(\mathbf{x}))] \tag{14}$$

$$\text{Subject to} : \begin{cases} g_1(\mathbf{x}) : PF(\mathbf{x}) \geq 0.95 \\ g_2(\mathbf{x}) : Q_c(\mathbf{x}) \leq Q_{c,max} \\ g_3(\mathbf{x}) : \eta_{ex}(\mathbf{x}) \leq \eta_{ex,max} \\ g_4(\mathbf{x}) : P_{safe}(\mathbf{x}|SVM) \geq 0.85 \\ \mathbf{x} \in \left[\mathbf{x}_{lower}, \mathbf{x}_{upper}\right] \end{cases} \tag{15}$$

In this constraint formulation, $g_1(\mathbf{x})$ enforces acoustic–mechanical–electrical matching by maintaining the power factor threshold ($PF(\mathbf{x}) \geq 0.95$). Constraints $g_2(\mathbf{x})$ and $g_3(\mathbf{x})$ act as relaxed numerical upper boundaries on the objective response space, explicitly specified as $Q_{c,max} = 16.0$ W and $\eta_{ex,max} = 0.18$ (18.0%). Across the convergent simulation samples gathered during Latin Hypercube Sampling and active learning iterations, the maximum recorded outputs were 13.65 W for cooling capacity and 15.67% for exergy efficiency. Set-

ting the upper bounds approximately 15–17% above these observed maxima provides sufficient exploration headroom for NSGA-II to search for superior trade-offs beyond the training dataset while effectively suppressing surrogate extrapolation overestimation. In sparsely sampled boundary regions, unconstrained Kriging models are prone to artificial response spikes; candidate points driven by these inflated values invariably trigger numerical divergence or transient negative absolute pressure in the compression space during Sage verification. Enforcing $g_2(\mathbf{x})$ and $g_3(\mathbf{x})$ prevents NSGA-II from converging toward these surrogate-induced artifacts without unduly restricting genuine performance improvements. Furthermore, $g_4(\mathbf{x})$ filters candidate solutions predicted to cause simulation failure or negative pressure based on the posterior probability from the SVM classifier ($P_{safe}(\mathbf{x}|\text{SVM}) \geq 0.85$). Following the initial parameter-space exploration by Latin Hypercube Sampling across the ranges in Table 3, this workflow operates as a constrained refinement confined to the numerically stable and convergent simulation domain. Finally, representative Pareto solutions are extracted for manual validation in Sage, comprising four anchor points (the maximum Q_c point, the maximum η_{ex} point, and two intermediate points at the 33rd and 66th percentiles along the Pareto front) and three alternative compromise candidates ranked by Technique for Order Preference by Similarity to Ideal Solution (TOPSIS) proximity (C_k, $k = 1, 2, 3$). If any of the four anchor points exhibits numerical non-convergence or negative compression-space pressure, the failed sample is appended to the infeasible dataset to retrain the SVM boundary. Concurrently, the alternative compromise candidates (C_k) serve as fallbacks to replace the primary TOPSIS solution if it encounters simulation failure. This verification procedure ensures that the final reported designs reside strictly within the convergent and numerically valid simulation domain.

Table 3. Sampling parameters and boundaries.

Parameters	Boundary	Parameters	Boundary
f (Hz)	[50, 65]	l_{reg} (m)	[0.03, 0.05]
α (N/A)	[12, 14]	D_{reg} (m)	[0.01, 0.013]
R_e (Ω)	[0.3, 0.7]	l_{pt} (m)	[0.03, 0.07]
V_{bs} (m^3)	$[3.1 \times 10^{-4}, 4.1 \times 10^{-4}]$	P_0 (P_a)	$[3 \times 10^6, 4 \times 10^6]$
M (kg)	[0.13, 0.17]	l_{it1} (m)	[1.3, 1.7]
V_{cs} (m^3)	$[2.6 \times 10^{-6}, 3.0 \times 10^{-6}]$	D_{it1} (m)	$[2.5 \times 10^{-3}, 3.5 \times 10^{-3}]$
l_{tt} (m)	[0.05, 0.15]	l_{it2} (m)	[1.7, 2.3]
D_{tt} (m)	$[3.8 \times 10^{-3}, 4.6 \times 10^{-3}]$	D_{it2} (m)	$[3.6 \times 10^{-3}, 4.5 \times 10^{-3}]$

The complete datasets, including the 16-dimensional Random Forest screening matrix, the initial 250 Latin Hypercube samples, the active learning iterative points, the SVM solvability boundary data, and the trained Kriging model binaries, are cataloged in the Supplementary Materials.

2.3. Optimization Process

Integrating the above methods, this study proposes a CPTC multi-parameter collaborative optimization architecture with physics-boundary awareness and adaptive closed-loop fault tolerance (Figure 6). Its implementation process consists of three core progressive stages:

- Phase I (Dimensionality Reduction and High-Precision Foundation Construction): The RF algorithm was utilized for feature importance ranking to reduce the design space to 10 core parameters. Subsequently, an initial global Kriging surrogate model was constructed combining LHS with a CEI-based batch active learning strategy.
- Phase II (Hybrid Feedback Correction and SVM Training): A hybrid feedback mechanism integrates Pareto-front verification and active learning to calibrate surrogate

accuracy. During this process, samples evaluated by Sage are classified into valid and invalid categories. The negative class comprises parameter combinations that trigger numerical divergence in the Sage root-finding solver or yield numerical artifacts (such as negative absolute pressure in the compression space). While numerical non-convergence in a one-dimensional solver does not necessarily prove real-world physical infeasibility, such points cannot provide valid thermodynamic responses to guide optimization. These invalid samples are, therefore, utilized to train a probabilistic SVM classifier. The resulting SVM boundary demarcates the numerically tractable and physically valid simulation domain, filtering candidate designs that could mislead the algorithm with divergent solutions.

- Phase III (Multiple Constraints and Robust Decision Implementation): To address potential divergence risks near thermodynamic limits, the final NSGA-II optimization integrated dual thermodynamic extremum constraints, SVM probabilistic filtering, and a rigid power factor constraint (PF $\geq$ 0.95). At the decision-making stage, a dual-track extraction strategy was employed, targeting four robust anchor points and three optimal compromise candidates. This approach incorporates an adaptive fallback mechanism to iteratively verify physical feasibility via the SVM, thereby mitigating convergence toward pseudo-optima and yielding verified, physically feasible Pareto optimal solutions.

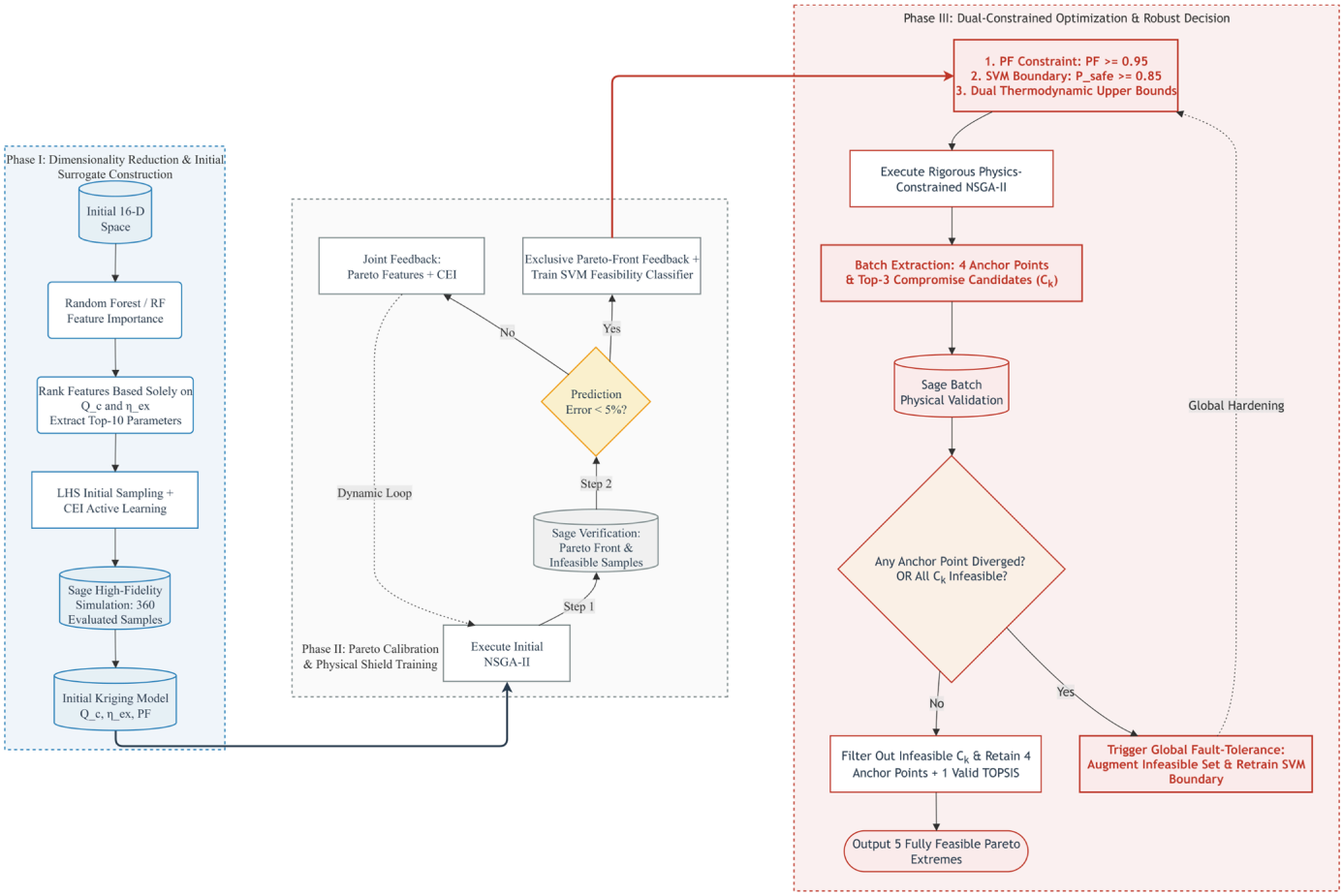


Figure 6. Flowchart of the proposed three-phase collaborative optimization framework integrating AcME coupling and physical boundary constraints (Phase I: RF dimensionality reduction and active Kriging surrogate construction; Phase II: hybrid Pareto calibration and SVM numerical solvability boundary training; Phase III: multi-constrained NSGA-II optimization with power factor ($PF \geq 0.95$) and dual thermodynamic upper bounds, followed by robust multi-candidate decision and fallback validation).

3. Results and Discussion

3.1. Quantification of Core Parameter Sensitivity and Analysis of the Acoustic–Mechanical–Electrical Coupling Mechanism

To restrict the 16-dimensional optimization within an engineering-feasible space, initial parameter boundaries (Table 3) were constrained by the AcME coupling mechanism and the following physical limits:

- Electromechanical dynamics: Operating frequency (f) and linear motor parameters are bounded by the resonance frequency band and mover overstroke safety margins.
- Thermodynamic and structural constraints: Inflation pressure (P_0) and spatial volumes (V_{bs}/V_{cs}) are restricted by shell stress limits and the working fluid's equation of state.
- Acoustic geometry and flow constraints: Channel length-to-diameter ratios (e.g., regenerator, transfer tube, inertance tubes) are constrained by viscous friction limits, acoustic impedance rebalancing intervals, and precision machining tolerances.

Prior to LHS, a pre-simulation screening via the Sage 1D model eliminated boundary combinations (e.g., negative compression space pressure, reverse gas flow) to ensure the physical validity of the 160 initial samples.

The 160 sets of valid physical simulation responses (Q_c, η_{ex} and PF) were input into the RF algorithm, and the variable influence was evaluated based on the OOB permutation model. Considering the compact layout and manufacturing guidelines of the CPTC, a coupling constraint on the inner diameters of the regenerator and pulse tube ($D_{reg} = D_{pt}$) was added to strip redundant dimensions. The normalized sensitivity scores reveal a clear physical hierarchical structure (as shown in Figure 7).As shown in Figure 8, the out-of-bag mean squared error rapidly stabilizes as the number of grown decision trees increases, verifying the convergence of the ensemble model.

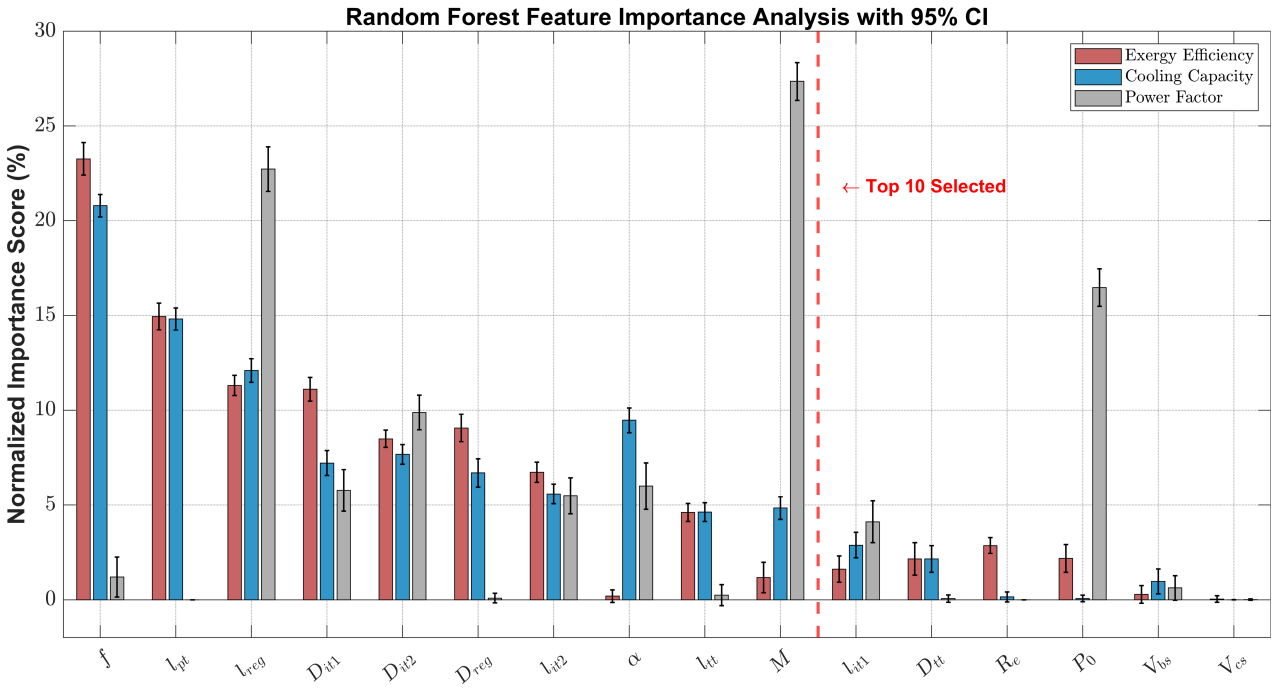


Figure 7. Normalized feature importance ranking of 16 candidate parameters across three performance metrics evaluated by the Random Forest algorithm.

Figure 7 illustrates the feature importance distribution with 95% confidence intervals. Based on the normalized importance scores, the RF model screened the core parameters dominating the system's thermodynamic performance and acoustic phase, and their sensi-

tivity distribution exhibits a significant physical hierarchy that can be summarized into the following three core physical dimensions:

1. Dominant layer of thermoacoustic conversion (f, l_{pt}, l_{reg}): The f occupies the dominant position in the feature importance ranking. The frequency not only determines the thermal penetration depth of the alternating fluid within the porous medium of the regenerator, directly affecting the gas–solid heat transfer efficiency, but it also serves as the dynamic baseline for establishing the cross-domain AcME network coupling, thereby determining the global resonance state of the system. In addition, the l_{pt} and l_{reg} are also highly sensitive: the former alters the cold-end compliance and dominates the cold-end acoustic phase shift; the latter restricts the irreversible friction game between the heat transfer area and the microscopic flow resistance.

2. Nonlinear tuning network of aerodynamic phase (D_{it1}, D_{it2}, D_{reg}, l_{it2}): Referring to the linear thermoacoustics fundamental equations proposed by Swift, the inductive impedance L and resistive impedance R_ν of the fluid in a pipe can be approximately expressed as:

$$L \simeq \frac{\rho_m \Delta x}{A} \tag{16}$$

$$R_\nu \simeq \frac{\mu \Pi \Delta x}{A^2 \delta_\nu} = \frac{\mu S}{A^2 \delta_\nu} \tag{17}$$

where ρ_m is the mean density, A is the cross-sectional area, Δx is the axial length, μ is the dynamic viscosity, Π and S are the perimeter and surface area, and δ_ν is the viscous penetration depth.

The data-driven results align with thermoacoustic theory: the inner diameter of the inertance tube determines the flow velocity of the working fluid inside the tube, and a contraction induces an increase in flow resistance, making it a primary parameter for tuning the phase difference. Further analysis indicates that increasing the length of the high-speed flow region adjacent to the pulse tube (l_{it1}) leads to an increase in viscous friction dissipation; this dimension was automatically eliminated during feature screening due to its resistive dissipation penalty. Conversely, increasing l_{it2} at the terminal end, where the flow velocity is attenuated, achieves inductive phase tuning at a lower dissipation cost. This feature selection corroborates the surrogate model's characterization of fluid dynamic dissipation mechanisms.

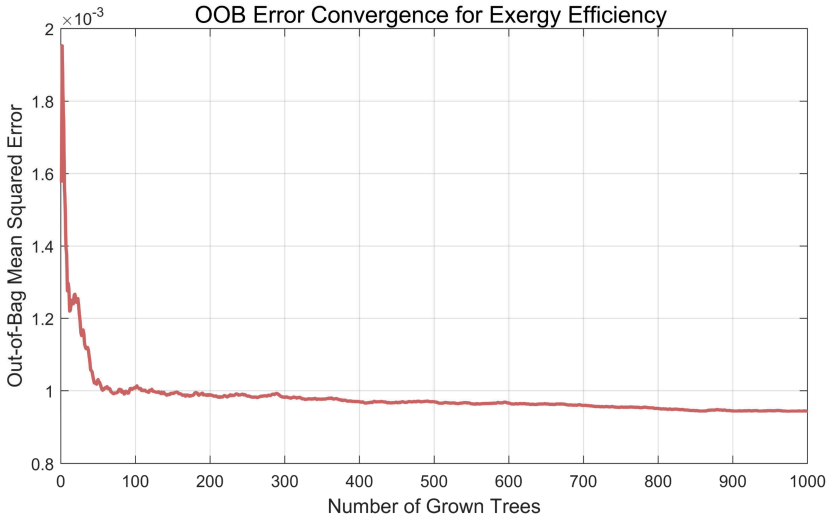


Figure 8. OOB mean squared error convergence curve for the η_{ex} prediction model versus the number of grown decision trees in the Random Forest ensemble.

3. Adaptive evolution of electromechanical coupling (α, l_{tt}, $\boldsymbol{M}$): The significant contributions of the α and m demonstrate the necessity of whole-system collaborative optimization encompassing dynamics. Under variable-frequency conditions, to satisfy the physical hard constraint of the global power factor (PF ≥ 0.95), the system must dynamically reconstruct M and α to match the natural resonance frequency $f_M = \frac{1}{2\pi}\sqrt{\frac{k_s}{M}}$ that deviates from the initial state. This reveals the cross-domain coupling mechanism, where acoustic load variations drive local phase shifts, and the electromechanical system evolves adaptively to stabilize electrical performance.

In contrast, the R_e, acting as a static background loss, lacks dynamic phase-tuning capability; parasitic parameters such as the V_{bs} and V_{cs}, as well as the inflation pressure (a macroscopic operating condition setting), were all marginalized in the ranking due to their low phase sensitivity.

3.2. Adaptive Construction and Kriging Surrogate Model

Based on the screened 10-dimensional feature subspace, an initial set of 250 LHS was evaluated via 1D Sage simulations within the numerically convergent domain to construct the Kriging surrogate models. A 5-fold cross-validation (5-fold CV) procedure, characterized by the coefficient of determination (R^2), root-mean-square error (RMSE), and 95% prediction confidence bands ($\pm 1.96\sigma$), was deployed to evaluate generalization accuracy.

Figure 9 presents the cross-validation performance comparison between the initial 250-sample baseline and the converged active learning model. As shown in Figure 9a, the initial model demonstrates satisfactory global fitting capability across the convergent parameter domain, yielding R^2 values of 0.9812 for Q_c, 0.9663 for η_{ex}, and 0.9366 for PF, with corresponding RMSE values of 0.3655 W, 0.0065, and 0.0048.

However, satisfactory global cross-validation metrics across a uniformly sampled 10-dimensional space do not guarantee reliable local fidelity during extreme multi-objective search. With 250 samples dispersed across a 10-dimensional hypercube, sample density remains inherently sparse along the narrow Pareto compromise corridor and multi-variable physical boundaries. When unrefined surrogates are coupled with evolutionary optimization, localized epistemic variance easily induces boundary extrapolation distortion, guiding algorithms toward pseudo-optima that trigger solver divergence upon physical verification.

To reinforce local frontier fidelity without exhaustive global sampling, a two-stage sequential refinement was implemented. First, two cycles of CEI active learning introduced 100 targeted infill samples focused along high-gradient regions and the impedance safety boundary ($PF \geq 0.95$), assembling a 350-sample surrogate to initialize the Phase III optimization. Subsequently, candidate solutions generated during the initial NSGA-II iterations were verified in Sage, and the resulting physical feedback samples were dynamically incorporated to calibrate localized surrogate gradients (Figure 6).

To provide a comprehensive assessment of the metamodeling methodology, Figure 9 compares the 5-fold cross-validation accuracy between the initial baseline surrogate (Figure 9a) and the final calibrated surrogate obtained after the closed-loop feedback process detailed in Section 3.3 and Figure 6 (Figure 9b).

Figure 9b presents the 5-fold cross-validation metrics of the resulting final calibrated model. Because the supplementary samples were concentrated within the localized Pareto compromise corridor and boundary thresholds rather than uniformly dispersed across the design volume, the global cross-validation metrics exhibit marginal variations (R^2 reaches 0.9918 for Q_c, 0.9830 for η_{ex}, and 0.9529 for PF, with RMSE values remaining at comparable levels). Nevertheless, as quantitatively verified in Section 3.3 and Table 4, this targeted calibration stabilizes boundary predictions, suppressing the initial 21.82% frontier

prediction discrepancy down to 0.38% and ensuring verifiable physical convergence across all final Pareto extremes.

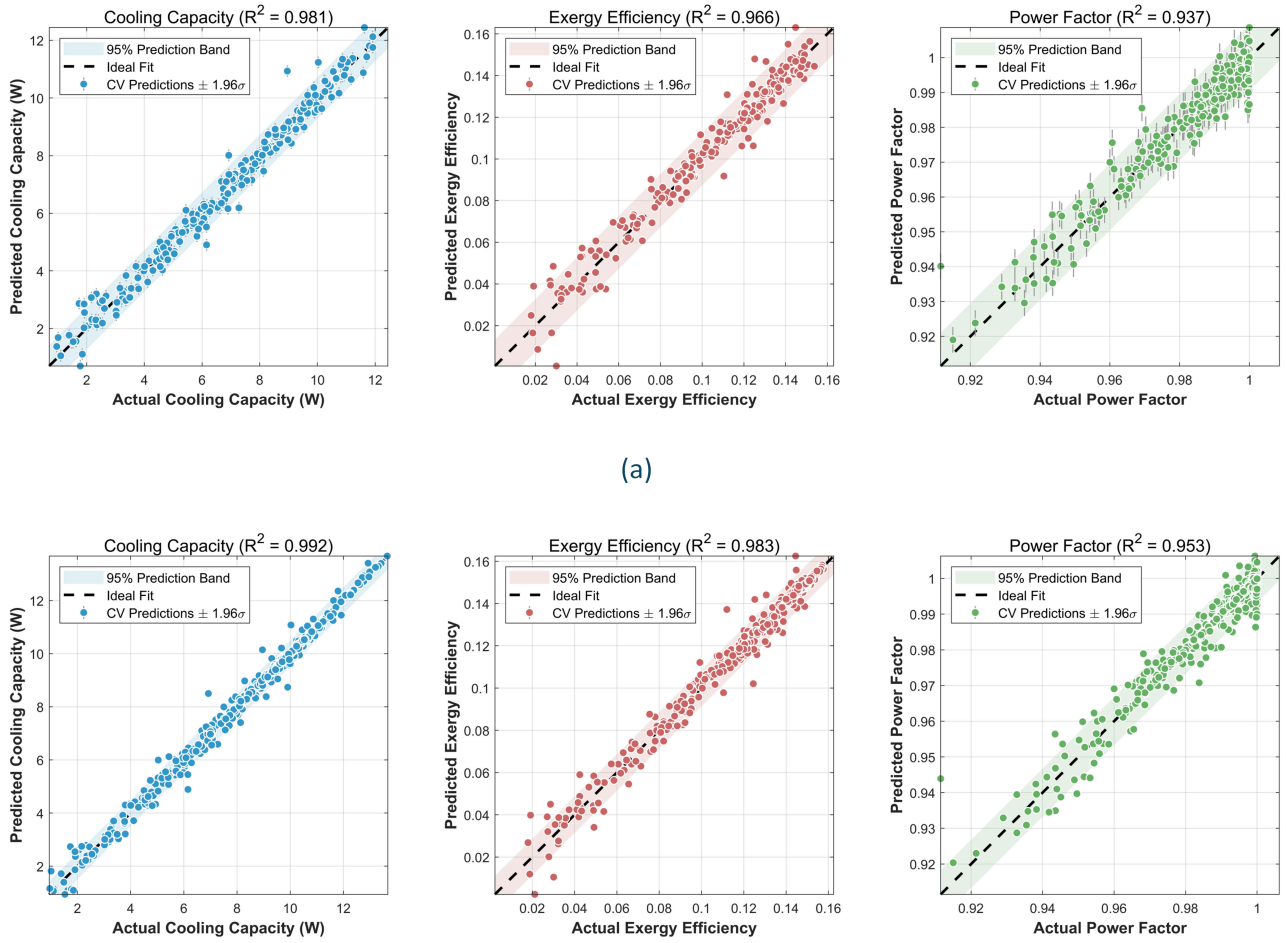


Figure 9. Five-fold cross-validation accuracy evolution of the Kriging surrogate models for Q_c, η_{ex} and PF: (**a**) initial surrogate model trained on 250 LHS samples; (**b**) final calibrated surrogate model incorporating active learning infill and iterative Pareto-front feedback (the dashed diagonal represents the ideal fit $y = x$; error bars denote $\pm 1.96\sigma$ cross-validation uncertainty; shaded regions indicate the 95% prediction confidence bands).

Table 4. Comparison of prediction accuracy for Pareto extremum and compromise points evaluated at the surrogate optimization stage (11-node coarse grid).

Optimization Stage	Feature Point	Q_c Pred. (W)	Q_c Valid. (W)	Error (%)	η_{ex} Pred. (-)	η_{ex} Valid. (-)	Error (%)	Physical Feasibility
Initial (Uncorrected)	Max Q_c	14.19	N/A	N/A	0.1685	N/A	N/A	Infeasible
	Max η_{ex}	13.15	11.16	17.85	0.1725	0.1424	21.14	Feasible
	TOPSIS	13.91	12.07	15.26	0.1715	0.1408	21.82	Feasible
Final (Converged)	Max Q_c	13.68	13.57	0.77	0.1496	0.1485	0.74	Feasible
	Max η_{ex}	11.49	11.5	0.06	0.1592	0.1583	0.57	Feasible
	TOPSIS	12.99	12.98	0.05	0.1569	0.1563	0.38	Feasible

Note: "Pred." denotes the Kriging surrogate model prediction, and "Valid." denotes the numerical validation using the Sage model with an 11-node coarse grid (consistent with the surrogate training set). "N/A" indicates that the simulation diverged and failed to output a valid result. The validated TOPSIS solution (Q_c = 12.98 W, η_{ex} = 15.63%) represents the coarse-grid numerical baseline for the selected optimal geometry prior to the fine-grid evaluation in Section 3.4.

3.3. NSGA-II Multi-Objective Optimization and Macroscopic Performance Evaluation

Based on the previously established and verified Kriging surrogate model, this study deployed the NSGA-II with an elite preservation strategy to simultaneously maximize the CPTC's cooling capacity and overall exergy efficiency and set the global power factor (PF $\geq$ 0.95) as a physical hard constraint.

In the preliminary stage of multi-objective exploration, the uncalibrated surrogate model (trained on the 350 samples assembled after LHS and initial CEI iterations, prior to Pareto-front feedback) inevitably faces boundary overestimation and selective bias along the complex trade-off boundary. As shown in Table 4, during this initial uncorrected stage, the predicted maximum cooling capacity configuration diverged during 1D physical verification in Sage (labeled "Infeasible"), while the predicted TOPSIS compromise solution exhibited a notable validation discrepancy of 21.82% in exergy efficiency. This discrepancy demonstrates that standard space-filling and variance-based active learning alone cannot completely suppress numerical artifacts along coupled thermodynamic boundaries.

In strongly coupled AcME systems, relying solely on boundary constraints without concurrent model recalibration tends to cause the evolutionary search to cycle across adjacent non-convergent regions. When the optimizer encounters an infeasible boundary, the epistemic uncertainty of the uncalibrated surrogate easily misleads the search trajectories toward neighboring, unmapped parameter subspaces that similarly trigger solver divergence or pressure artifacts. To mitigate these boundary oscillations, the Phase II calibration deploys an active learning procedure that couples CEI infilling with Pareto-frontier validation (Figure 6). Supplementing high-fidelity numerical evaluations directly along the multi-objective trade-off interface provides localized gradient information, while the SVM boundary ($P_{safe} \geq 0.85$) effectively blocks divergent domains. As illustrated in Figure 10, this synergistic formulation progressively suppresses surrogate extrapolation tendencies, guiding the algorithm toward a physically validated, continuous Pareto front.

The resulting Pareto front clearly demonstrates the fundamental thermodynamic trade-off in the CPTC between cooling capacity (Q_c) and overall exergy efficiency (η_{ex}). Pushing for higher cooling capacities requires elevated alternating mass flow rates and dynamic pressure ratios, which intensifies microscopic viscous shear and radial heat transfer irreversibilities within the porous regenerator and pulse tube, yielding a monotonic decline in overall exergy efficiency. Furthermore, theoretical extremes along the upper boundaries often approach the fluid dynamic stability limits of the system, where pronounced transient pressure fluctuations risk triggering negative absolute pressure in the compression space.

To balance peak thermodynamic performance with engineering stability, candidate solutions were screened using the multi-candidate extraction strategy outlined in Section 2.2.4. Constrained by the power factor requirement ($PF \geq 0.95$) and the SVM solvability shield, the optimal compromise point extracted by TOPSIS decision making achieved verified numerical convergence: under 1D Sage coarse-grid validation (11 nodes), net cooling capacity reached 12.98 W and exergy efficiency reached 15.63%, with surrogate prediction discrepancies confined to 0.05% and 0.38%, respectively. This validated TOPSIS configuration establishes the numerical baseline for the subsequent 50-node fine-grid thermodynamic and cascaded exergy evaluation detailed in Section 3.4.

3.4. Comparative Evaluation of Thermodynamic Performance and Exergy Destruction

Based on the multi-physics coupling and energy cascade transfer mechanisms, combined with the Sage model of the regenerator and pulse tube components utilizing a 50-node fine grid, this section conducts a comprehensive and in-depth comparative evaluation of the models before and after optimization. By adjusting the core geometric parameters of

the system, the acoustic matching characteristics of the entire machine are reconstructed, thereby significantly enhancing the cooling capacity and overall exergy efficiency.

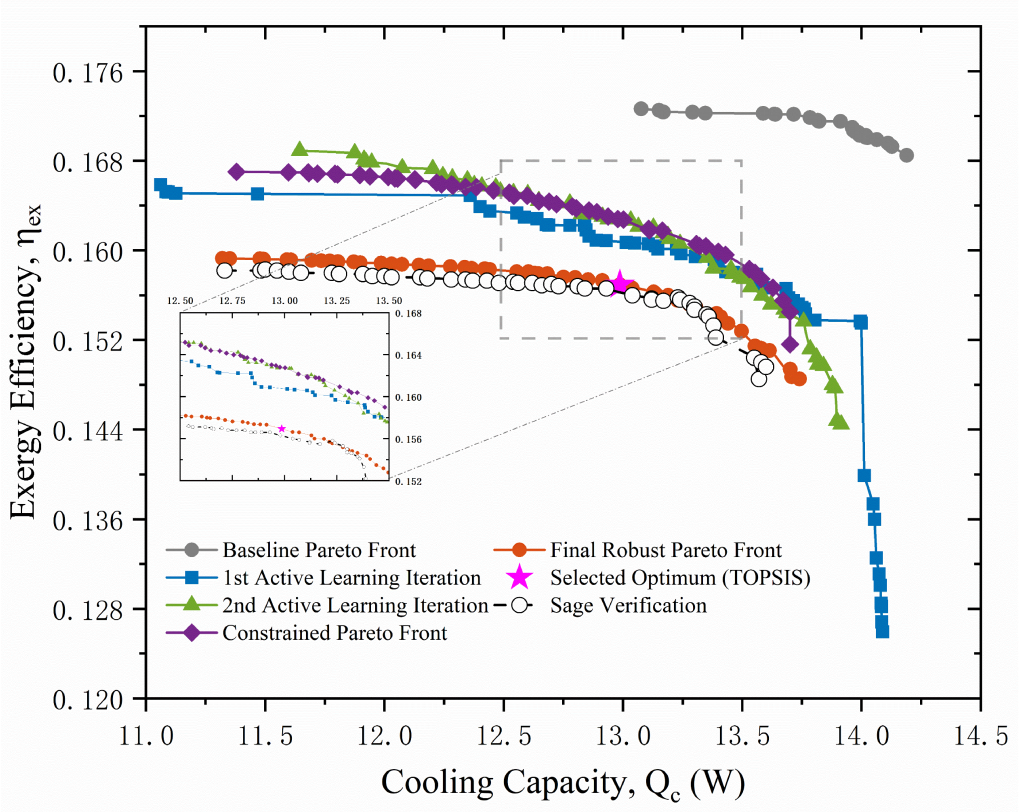


Figure 10. Pareto front evolution between Q_c and η_{ex} during surrogate active learning and constrained optimization under the 11-node coarse grid (the inset magnifies the trade-off compromise region; open circles denote 1D physical Sage validation points along the front; the star marks the compromise optimum selected by the TOPSIS decision method).

3.4.1. Impact Mechanism of Core Geometric Parameter Regulation on Thermodynamic and Acoustic Field Characteristics

Table 5 presents the optimal geometric parameters and the corresponding thermodynamic performance under the 50-node fine-grid verification. Compared with the coarse-grid results obtained during the optimization stage (Table 4), the fine-grid spatial discretization resolves the steep axial temperature gradients across the regenerator more accurately and suppresses artificial numerical dissipation. Consequently, the verified net cooling capacity of the TOPSIS design is refined to 14.41 W, with an exergy efficiency of 17.65%. Constrained by the $PF \geq 0.95$ requirement and the SVM feasibility boundary, the algorithm identifies an optimal structural configuration while avoiding numerical instability. Specifically, the transfer tube is significantly shortened (l_{tt} reduced by 49.30%), and the pulse tube volume is expanded (l_{pt} increased by 18.60%). This geometric reconfiguration effectively modulates the cross-component impedance.

The volumetric expansion of the pulse tube enhances the local acoustic compliance. Concurrently, the shortened transfer tube reduces the fluid inertance and viscous contact area, yielding an 11.86% decrease in acoustic resistance (R_a). This combination dynamically shifts the acoustic field within the regenerator toward a traveling-wave phase. Consequently, the hot-end phase angle (φ_h) shifts from 2.398° to 21.14°, and the cold-end phase angle (φ_c) improves from 29.69° to 18.18°. Under the premise of AcME matching, these phase optimizations mitigate internal dissipative losses. Ultimately, the Q_c at 80 K increases from 9.425 W to 14.41 W, and the η_{ex} rises from 14.65% to 17.65%.

Table 5. Comparison of optimal geometric parameters and fine-grid numerical performance (50 nodes) between the baseline model and the optimized model.

Parameters/Performance (Unit)	Initial Baseline	Optimized Trade-Off	Variation (%)
I. Top 10 Core Geometric Parameters			
f (Hz)	60	64.1	6.83
l_{pt} (m)	0.05	0.0593	18.60
l_{reg} (m)	0.04	0.0431	7.75
D_{it1} (m)	0.003	0.00283	−5.67
D_{it2} (m)	0.004	0.00445	11.25
D_{reg} (m)	0.0114	0.01214	6.49
l_{it2} (m)	2.049	2.1951	7.13
α (N/A)	13.2	13.9451	5.64
l_{tt} (m)	0.1	0.0507	−49.30
M (kg)	0.15	0.1416	−5.60
II. Core Thermodynamic Performance Metrics			
η_{ex} (−)	0.1465	0.1765	20.48
W_e (W)	176.9	224.6	26.96
Q_c (W)	9.425	14.41	52.89
PF (−)	0.987	0.9942	0.73
III. Underlying Acoustic Coupling Analysis			
η_c (−)	0.1825	0.2184	19.67
η_{co} (−)	0.8027	0.8080	0.66
φ_h (°)	2.398	21.14	781.57
φ_c (°)	−29.69	−18.18	−38.77
P_r	1.273	1.326	4.16
Ra (Pa·s/m^3)	4.292×10^8	3.783×10^8	−11.86
Xa (Pa·s/m^3)	-9.424×10^7	-1.854×10^8	96.73
$Z = \sqrt{{R_a}^2 + {X_a}^2}$	4.394×10^8	4.213×10^8	−4.12

Note: The geometric parameters of the optimized design correspond strictly to the TOPSIS compromise solution selected in Section 3.3. The performance metrics (Q_c = 14.41 W, η_{ex} = 17.65%) are evaluated using the 50-node fine-grid Sage model; the improvement over the coarse-grid values in Table 4 (12.98 W, 15.63%) is attributed to the accurate resolution of axial temperature gradients and the suppression of artificial numerical dissipation. Structural parameters are rounded to standard engineering manufacturing tolerances (axial lengths to 0.1 mm, radial dimensions to 0.01 mm, and frequency to 0.1 Hz). The deviation in performance feedback between this prior rounded solution in Sage simulation and the algorithm's original floating-point solution is less than 0.1%, balancing theoretical optimality and manufacturing feasibility.

3.4.2. Multi-Physical Domain Cascaded Exergy Analysis and Detailed Evaluation of Exergy Destruction in Refrigeration Components

Based on the cascaded energy flow analysis (Table 6) and the microscopic exergy destruction breakdown (Figure 11), the geometric optimization results in a redistribution of irreversible losses. As detailed in Table 6, the optimized model exhibits an increased total electrical power input (W_e), rising from 177.0 W to 224.6 W. Consequently, the absolute exergy destruction within individual components increases due to the expanded energy throughput. To evaluate the underlying thermodynamic irreversibilities objectively, the relative exergy destruction ratio, normalized against W_e, is analyzed.

Table 6. Multi-domain cascaded exergy breakdown and acoustic exergy destruction under 50-node fine-grid evaluation before and after optimization.

Exergy Cascade and Components	Baseline (W)	Base (% of W_e)	Optimized (W)	Opt (% of W_e)	Remarks
I. Electrical Domain					
W_e	176.9	100%	224.6	100%	Electrical energy input
$E_{d,e}$	17.60	9.95%	17.60	7.84%	Coil resistance
$W_{e,net}$	159.30	90.05%	207.00	92.16%	Electromechanical conversion
II. Mechanical Domain					
$E_{d,m}$	17.30	9.78%	25.60	11.39%	Moving mass friction
$W_{pv,in}$	142.00	80.27%	181.40	80.77%	Gross acoustic driving power
III. Acoustic Domain Exergy Destruction (Losses)					
Transfer Tube	6.24	3.53%	7.96	3.54%	Viscous friction dominated
Dead Space	5.61	3.17%	7.59	3.38%	Heat transfer dominated
Regenerator	48.46	27.40%	63.2	28.14%	See Figure 11 for micro-mechanisms
Pulse tube	14.44	8.16%	11.98	5.33%	See Figure 11 for micro-mechanisms
Inertance Tubes1	11.70	6.61%	16.30	7.26%	Phase-shifting penalty
Inertance Tubes2	8.31	4.70%	6.19	2.76%	Phase-shifting penalty
HX, Solid-Wall and Residuals	21.32	12.05%	28.55	12.71%	Uncalculated secondary dissipations
IV. Overall Output					
Q_c	9.425		14.41		Macroscopic cooling power
E_c	25.92	14.65%	39.63	17.65%	$E_c = Q_c \times \left(\frac{300}{80} - 1\right)$

Note: Both baseline and optimized cases are evaluated using the 50-node fine-grid model. The linear motor operates under a fixed-current model assumption; consequently, the coil Joule dissipation remains identical between cases, and the increase in W_e is transferred entirely into electromechanical conversion power ($W_{e,net}$). This increment is governed by the combined effects of the increased motor constant α, the frequency shift, and the altered piston mover dynamics under the coupled load. All values in Part III of Table 6 represent component exergy destructions (E_d). Exergy destruction terms are presented both as absolute values (in Watts) and as normalized ratios relative to the total active electrical input power (% of W_e). For the detailed microscopic breakdown (e.g., $E_{d,\mathrm{fric}}$, $E_{d,Qw}$, $E_{d,Qx}$) of the acoustic domain, please refer to Figure 11.

In the electrical domain, guided by the PF $\geq$ 0.95 requirement, the adjustment in electromechanical conversion reduces the proportion of coil Joule heat loss from 9.95% to 7.84%, which elevates the $W_{pv,in}$ to 181.40 W. In the acoustic domain, the components exhibit the following dissipation variations:

- Regenerator: The reduction in void volume increases the working fluid velocity, which elevates viscous friction exergy destruction but increases gas–solid heat transfer. Consequently, axial static heat conduction ($E_{d,Qx}$) decreases from 8.19% to 6.2%, forming a structural trade-off.
- Pulse Tube: The geometric volume expansion reduces momentum shear near the tube wall, lowering both friction dissipation and local heat transfer, thereby preserving the cooling capacity.
- Phase-Tuning Components: The inertance tube group demonstrates a spatial shift in exergy destruction, characterized by an increase at the front end (IT1: 6.61% to 7.26%) and a decrease at the terminal end (IT2: 4.70% to 2.76%). This redistribution corresponds to the microscopic phase-shifting penalty associated with the global acoustic impedance realignment.

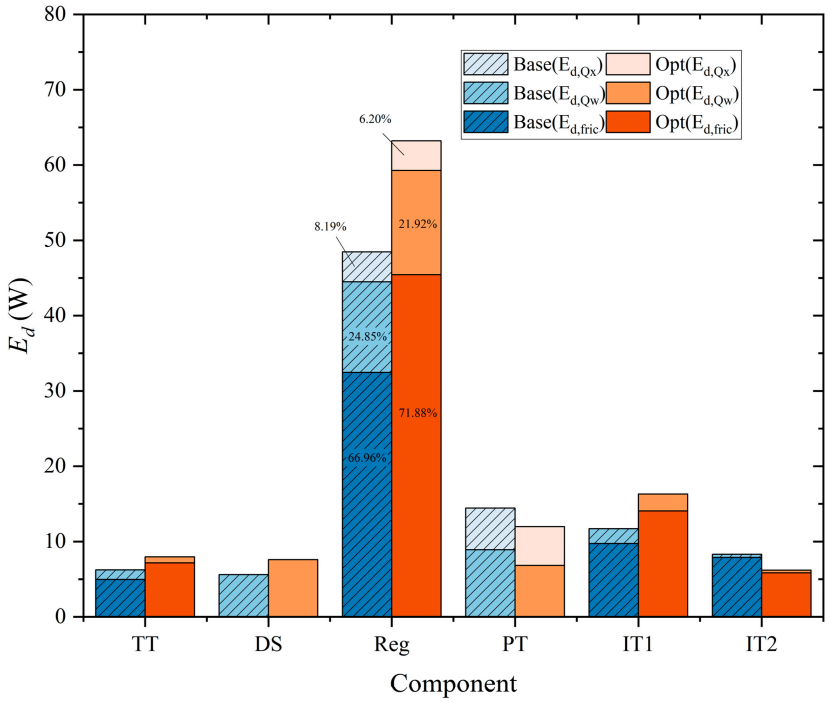


Figure 11. Comparison of microscopic exergy destruction across acoustic components between the baseline and optimized CPTC models evaluated under the 50-node fine-grid Sage simulation at 80 K (component designations: TT: transfer tube; DS: dead space; Reg: regenerator; PT: pulse tube; IT1/IT2: first- and second-stage inertance tubes. Stacked loss: $E_{d,\mathrm{fric}}$, $E_{d,Qw}$, and $E_{d,Qx}$ represent viscous friction dissipation, radial gas-wall heat transfer loss, and axial thermal conduction loss, respectively; percentage callouts indicate the relative internal dissipation proportions within the regenerator).

4. Conclusions

To address multi-parameter coupling, complex impedance matching, and extrapolation distortion in the high-dimensional optimization of CPTCs, this study proposed a data-driven collaborative framework based on the AcME impedance matching mechanism. Departing from previous studies that optimized isolated cold fingers across four to eight variables using static surrogate models without compressor dynamic coupling, this framework achieves constrained multi-parameter collaborative optimization across an integrated 10-dimensional design space. The main methodological conclusions and thermodynamic findings are as follows:

1. Feature screening and dimensionality reduction: The Random Forest algorithm evaluated out-of-bag permutation importance to isolate dominant thermoacoustic parameters (f, l_{pt}, l_{reg}), aerodynamic phase-tuning parameters ($D_{it1}, D_{it2}, D_{reg}, l_{it2}$), and electromechanical parameters (α, l_{tt}, M). This systematically compressed the design space from 16 initial dimensions to 10 core variables, reducing the sample scale and computational overhead for subsequent modeling.
2. Surrogate accuracy improvement over static benchmarks: Across the initial 250 convergent Latin Hypercube samples, the Kriging surrogate achieved baseline determination coefficients of $R^2 = 0.9812$ for Q_c and $R^2 = 0.9663$ for η_{ex}. Although expanding the dataset to 350 samples via initial CEI active learning improved global coverage, deploying this uncalibrated surrogate in multi-objective exploration still exhibited boundary extrapolation discrepancies—inducing numerical solver divergence at the maximum cooling capacity configuration and an initial coarse-grid TOPSIS validation error of 21.82% for exergy efficiency. Relying exclusively on boundary constraints without concurrent model recalibration causes search trajectories to cycle across ad-

jacent non-convergent parameter domains. Integrating sequential active learning (coupling CEI infilling with Pareto feedback in Phase II) with a probabilistic SVM solvability boundary ($P_{safe} \geq 0.85$, Phase III) provides essential localized gradient information. This combined formulation prevents search oscillations across solver failure domains and suppresses the final coarse-grid validation discrepancies to 0.05% for Q_c and 0.38% for η_{ex}.

3. Mitigation of numerical divergence via boundary constraints: Unconstrained global exploration in high-dimensional spaces easily enters regimes that trigger 1D solver divergence or compression-space negative absolute pressure. By deploying a probabilistic Support Vector Machine classifier ($P_{\text{safe}} \geq 0.85$) to delineate the numerically solvable simulation domain, alongside enforcing a power factor threshold ($PF \geq 0.95$) as a robustness safeguard against extrapolation, the search was confined to computationally stable regions, effectively mitigating the risk of converging toward pseudo-optima.
4. Cross-domain impedance reconstruction and performance enhancement: Simulation under the 50-node fine-grid Sage model at 80 K, the η_{ex} increased from 14.65% to 17.65%, yielding a net cooling capacity of 14.41 W. Microscopic analysis confirms that balancing viscous dissipation (via shortened transfer tubes) and mechanical resonance (via frequency adjustment) with electromagnetic parameter reconstruction is a viable pathway to re-match the global AcME phase.

Limitations and Future Work:

While this 1D physical-data collaborative framework efficiently demarcates optimal parameter spaces and eliminates inefficient regions, it inherently simplifies complex internal flow fields. Phenomena such as 3D eddy dissipation, high-frequency Rayleigh streaming, and boundary layer dynamics at abrupt geometric cross-sections require higher-fidelity modeling. Based on the candidate solution pool generated in this study, future work will conduct 3D computational fluid dynamics (CFD) validations on localized geometric transitions, alongside relevant experimental validations to verify the optimized designs.

Supplementary Materials: The following supporting information can be downloaded at: https://www.mdpi.com/article/10.3390/en19194639/s1, Figure S1. Graphical configuration interface of the 1D Sage solver (Solver tab in Sage Options), showing the step-size restriction adjusted toward the stable regime and the corresponding convergence tolerance settings. Table S1. Comprehensive computational hyperparameters and algorithmic configurations of the multi-stage collaborative optimization framework. Table S2. Organization and file inventory of the accompanying (Simulation Data and Trained Surrogates) directory.

Author Contributions: R.L.: conceptualization, methodology, software, formal analysis, investigation, data curation, writing—original draft; C.Z.: validation, methodology, writing—review and editing; C.Y.: supervision, project administration, writing—review and editing; H.D.: software, data curation; B.W.: software, validation, writing—review and editing, funding acquisition. All authors have read and agreed to the published version of the manuscript.

Funding: This work was financially supported by the National Natural Science Foundation of China (Grant No. 52476020).

Data Availability Statement: The data and models supporting the findings of this study—including the design matrices, rejected infeasible samples, active learning datasets, trained surrogate models, and Sage numerical model files—are openly available in the Supplementary Materials accompanying this article.

Conflicts of Interest: The authors declare no conflicts of interest.

Nomenclature

A	Area (m^2)
C	Capacitance (F)
D	Diameter (m)
E	Exergy rate (W)
f	Operating frequency (Hz)
F	Force amplitude (N)
h	Specific enthalpy (J/kg)
I	Motor driving current (A)
j	Imaginary unit ($\sqrt{-1}$)
k_s	Mechanical spring stiffness (N/m)
l	Axial length (m)
L	Acoustic inertance per unit length ($Pa \cdot s^2/m^4$)
L_e	Motor coil inductance (H)
M	Piston mover mass (kg)
$\dot{m}$	Mass flow rate (kg/s)
P	Dynamic pressure amplitude (Pa)
P_0	Mean charging pressure (Pa)
PF	System electrical power factor (−)
P_r	Pressure ratio (−)
P_{safe}	Physical safety probability predicted by SVM (−)
Q	Heat flow (W)
Q_c	Cooling capacity at 80 K (W)
R	Specific gas constant ($J/(kg \cdot K)$); or resistance/damping (Ω, $Pa \cdot s/m^3$, $N \cdot s/m$)
S	Wetted surface area (m^2)
T	Absolute thermodynamic temperature (K)
u	Piston mover velocity (m/s)
U	Dynamic volume flow rate (m^3/s)
V	Supply voltage (V); or component volume (m^3)
W	Active electrical/acoustic power (W)
X	Reactance ($Pa \cdot s/m^3, N \cdot s/m, \Omega$)
Z	Impedance ($Pa \cdot s/m^3, N \cdot s/m, \Omega$)
Greek Symbols	
α	Motor force constant (N/A)
β	Phase angle of electromagnetic force to velocity ($^\circ$)
γ	Specific heat ratio (−)
Δx	Axial differential control volume length (m)
δ_v	Viscous penetration depth (m)
η	Efficiency
θ_{V-I}	Phase angle of the global equivalent impedance
μ	Dynamic viscosity ($Pa \cdot s$)
Π	Wetted perimeter (m)
ρ_m	Mean working fluid density (kg/m^3)
σ	Kriging surrogate prediction standard deviation
τ	Period of one operating cycle (s)
$\Phi(\cdot)$	Standard normal cumulative distribution function
φ	Acoustic phase angle ($^\circ$)
ψ	Phase angle of current to back-EMF ($^\circ$)
ω	Angular operating frequency (rad/s)
Subscripts	
0	Ambient or mean operating condition
a, m, e	Acoustic, mechanical, and electrical domains
bs, cs, co	Back space, compression space, and compression chamber
c,h	Cold end, hot end

d	Exergy destruction
ex	Exergy-related metric
fric,*Qw*,*Qx*	Viscous friction, radial heat transfer, and axial conduction
in,*out*,*net*	Inlet, outlet, and net converted quantities
*it*1,*it*2	First- and second-stage inertance tubes
pt,*reg*,*tt*	Pulse tube, regenerator, and transfer tube
pv	PV acoustic work
rms	Root-mean-square amplitude

Abbreviations

AcME	Acoustic–mechanical–electrical
ANN	Artificial neural network
CEI	Constrained Expected Improvement
CFD	Computational fluid dynamics
CHX	Cold heat exchanger
CPTC	Coaxial pulse tube cryocooler
CV	Cross-validation
DS	Dead space
EGM	Entropy generation minimization
EI	Expected improvement
EMF	Electromotive force
HHX	Hot heat exchanger
IT1	Firsts-stage inertance tube
IT2	second-stage inertance tube
LHS	Latin Hypercube Sampling
NGAS	Northrop Grumman Space Technology
NSGA-II	Non-dominated sorting genetic algorithm II
OOB	Out of bag
PF	Power factor
PoF	Probability of feasibility
PSO	Particle swarm optimization
PT	Pulse tube
PTC	Pulse tube cryocooler
Reg	Regenerator
RF	Random forest
RMSE	Root-mean-square error
RSM	Response surface methodology
SVM	Support Vector Machine
TOPSIS	Technique for order preference by similarity to ideal solution
TT	Transfer tube

References

1. Gifford, W.E.; Longsworth, R.C. Pulse-tube refrigeration. *J. Eng. Ind.* **1964**, *86*, 264–268. [CrossRef]
2. Pan, M.; Wang, N.; Yang, B.; Li, Y.; Tian, B.; Li, G.; Quan, J.; Zhao, M. Investigation on a 40 K high-frequency lightweight pulse tube cryocooler for space applications. *Cryogenics* **2025**, *151*, 104187. [CrossRef]
3. Yang, B.; Liu, Z.; Pan, M.; Tian, B.; Quan, J.; Ma, Y.; Liu, Y.; Chen, H.; Zhao, M.; Liang, J. A 600 mW@20 K thermally-coupled two-stage pulse tube precooler for space 4 K JT cryocooler reaches high efficiency with double-inlet phase shifter. *Cryogenics* **2025**, *148*, 104075. [CrossRef]
4. Zhang, A.; Wu, Y.; Liu, S.; Liu, B.; Yang, B. High-efficiency 3 W/40 K single-stage pulse tube cryocooler for space application. *Cryogenics* **2018**, *90*, 41–46. [CrossRef]
5. Rana, H.; Abolghasemi, M.A.; Stone, R.; Dadd, M.; Bailey, P. Numerical modelling of a coaxial Stirling pulse tube cryocooler with an active displacer for space applications. *Cryogenics* **2020**, *106*, 103048. [CrossRef]
6. Petach, M.; Waterman, M.; Tward, E.; Bailey, P.B. Pulse tube microcooler for space applications. *Cryocoolers* **2007**, *14*, 89–93.

7. Petach, M.; Waterman, M.; Pruitt, G.; Tward, E. High frequency coaxial pulse tube microcooler. *Cryocoolers* **2009**, *15*, 97–103.
8. Hu, J.Y.; Zhang, L.M.; Zhu, J.; Chen, S.; Luo, E.C.; Dai, W.; Li, H.B. A high-efficiency coaxial pulse tube cryocooler with 500W cooling capacity at 80K. *Cryogenics* **2014**, *62*, 7–10. [CrossRef]
9. Wang, N.; Zhao, M.; Ou, Y.; Zhu, Q.; Wei, L.; Chen, H.; Cai, J.; Liang, J. A high efficiency coaxial pulse tube cryocooler operating at 60 K. *Cryogenics* **2018**, *93*, 48–50. [CrossRef]
10. Tian, B.; Tang, Q.; Liu, C.; Ma, J.; Niu, Y.; Yang, B.; Li, R.; Ma, Y.; Zhao, M.; Cai, J. Characterization of the high-frequency performance of a coaxial Stirling-type pulse tube cryocooler at 60 K. *Appl. Therm. Eng.* **2026**, *284*, 129062. [CrossRef]
11. Radebaugh, R.; Garaway, I.; Veprik, A.M. Development of miniature, high frequency pulse tube cryocoolers. *Proc. SPIE* **2010**, *7660*, 76602J. [CrossRef]
12. Bao, D.; Tan, J.; Zhang, L.; Gao, Z.; Zhao, Y.; Dang, H. A two-dimensional model of regenerator with mixed matrices and experimental verifications for improving the single-stage Stirling-type pulse tube cryocooler. *Appl. Therm. Eng.* **2017**, *123*, 1278–1290. [CrossRef]
13. Yang, B.; Xi, X.; Gao, Z.; Chen, L.; Wang, J. A 3.27 K high-frequency pulse tube cryocooler using adsorbed 4He as part of the regenerator material. *J. Low Temp. Phys.* **2023**, *210*, 393–405. [CrossRef]
14. Jiang, Z.; Shen, J.; Li, S.; Wang, Y.; Zhang, H.; Wu, Y. Influence of frequency and pressure on entropy production characteristics of regenerator at 20 K pulse tube cryocooler. *Int. J. Refrig.* **2022**, *144*, 222–230. [CrossRef]
15. Radebaugh, R.; Lewis, M.; Luo, E.C.; Pfotenhauer, J.M.; Nellis, G.F.; Schunk, L.A. Inertance tube optimization for pulse tube refrigerators. *AIP Conf. Proc.* **2006**, *823*, 59–67. [CrossRef]
16. You, X.; Qiu, L.; Zhang, H.; Xin, Y.; Lu, J. Study on the impedance characteristics of a high-capacity pulse tube cryocooler. *Energy Rep.* **2022**, *8*, 2210–2218. [CrossRef]
17. Wakeland, R.S. Use of electrodynamic drivers in thermoacoustic refrigerators. *J. Acoust. Soc. Am.* **2000**, *107*, 827–832. [CrossRef] [PubMed]
18. Swift, G.W. *Thermoacoustics: A Unifying Perspective for Some Engines and Refrigerators*, 2nd ed.; Springer International Publishing: Cham, Switzerland, 2017. [CrossRef]
19. Dai, W.; Luo, E.; Wang, X.; Wu, Z. Impedance match for Stirling type cryocoolers. *Cryogenics* **2011**, *51*, 168–172. [CrossRef]
20. Gan, Z.; Wang, L.; Zhao, S.; Song, Y.; Wang, W.; Wu, Y. Acoustic impedance characteristics of linear compressors. *J. Zhejiang Univ. Sci. A* **2013**, *14*, 494–503. [CrossRef]
21. Rout, S.K.; Choudhury, B.K.; Sahoo, R.K.; Sarangi, S.K. Multi-objective parametric optimization of inertance type pulse tube refrigerator using response surface methodology and non-dominated sorting genetic algorithm. *Cryogenics* **2014**, *62*, 71–83. [CrossRef]
22. Rout, S.K.; Sahoo, R.K. Optimal design of orifice pulse tube refrigerator based on response surface and genetic algorithm. *Arab. J. Sci. Eng.* **2015**, *41*, 1735–1755. [CrossRef]
23. Panda, D.; Rout, S.K. Optimization of an inertance pulse tube refrigerator using the particle swarm optimization algorithm. *Heat Transf. Asian Res.* **2019**, *48*, 3508–3537. [CrossRef]
24. Panda, D.; Kumar, M.; Satapathy, A.K.; Sarangi, S.K.; Sahoo, R.K. Performance evaluation of a GM-type double inlet pulse tube refrigerator using artificial intelligence approach with experimental validation. *Arab. J. Sci. Eng.* **2020**, *45*, 9579–9597. [CrossRef]
25. Zhao, H.; Shao, W.; Cui, Z.; Zheng, C. Multi-objective parameter optimization of pulse tube refrigerator based on Kriging metamodel and non-dominated ranking genetic algorithms. *Energies* **2023**, *16*, 2736. [CrossRef]
26. Wang, Y.; Yan, Y.; Wang, R.; Cao, Z.; Cui, Z.; Zheng, C. Multi-dimensional flow simulation analysis and Kriging-based optimization study on thermodynamic process mechanism of pulse tube refrigerator with displacer. *Case Stud. Therm. Eng.* **2024**, *56*, 104216. [CrossRef]
27. Geng, Z.; Shao, W.; Cui, Z.; Zheng, C. Study on phase-shift mechanism and Kriging-based global optimization of the active displacer pulse tube refrigerators. *Energies* **2023**, *16*, 4263. [CrossRef]
28. Peherstorfer, B.; Willcox, K.; Gunzburger, M. Survey of multifidelity methods in uncertainty propagation, inference, and optimization. *SIAM Rev.* **2018**, *60*, 550–591. [CrossRef]
29. Bejan, A. *Entropy Generation Minimization: The Method of Thermodynamic Optimization of Finite-Size Systems and Finite-Time Processes*; CRC Press: Boca Raton, FL, USA, 1995.
30. Razani, A.; Roberts, T.; Flake, B. A thermodynamic model based on exergy flow for analysis and optimization of pulse tube refrigerators. *Cryogenics* **2007**, *47*, 166–173. [CrossRef]
31. Radebaugh, R. Thermodynamics of regenerative refrigerators. In *Generation of Low Temperature and Its Applications*; Ohtsuka, T., Ishizaki, Y., Eds.; Shonan Tech. Center: Kamakura, Japan, 2003; pp. 1–20.
32. Wang, B.; Guo, Y.; Chao, Y.; Wang, Y.; Wang, L.; Gan, Z. Acoustic-Mechanical-Electrical (AcME) coupling between the linear compressor and the Stirling-type cryocoolers. *Int. J. Refrig.* **2019**, *100*, 175–183. [CrossRef]
33. Breiman, L. Random forests. *Mach. Learn.* **2001**, *45*, 5–32. [CrossRef]

34. Janitza, S.; Hornung, R. On the overestimation of random forest's out-of-bag error. *PLoS ONE* **2018**, *13*, e0201904. [CrossRef] [PubMed]
35. Deb, K.; Pratap, A.; Agarwal, S.; Meyarivan, T. A fast and elitist multiobjective genetic algorithm: NSGA-II. *IEEE Trans. Evol. Comput.* **2002**, *6*, 182–197. [CrossRef]

Disclaimer/Publisher's Note: The statements, opinions and data contained in all publications are solely those of the individual author(s) and contributor(s) and not of MDPI and/or the editor(s). MDPI and/or the editor(s) disclaim responsibility for any injury to people or property resulting from any ideas, methods, instructions or products referred to in the content.